Bidirectional Soft Switching Push–Pull Resonant Converter Over Wide Range of Battery Voltages

Jong-Won Lim, *Student Member, IEEE*, Jamil Hassan, *Student Member, IEEE*, and Minsung Kim, *Senior Member, IEEE*

***Abstract*—This article presents a bidirectional soft-switching push–pull resonant converter that is highly efficient over a wide range of battery voltages. It is derived by integrating a current-fed push–pull circuit and an active voltage doubler circuit with a bidirectional switch. The converter operates as a pulsewidth modulation (PWM) current-fed push–pull resonant-boost converter in the forward direction, but as a PWM half-bridge resonant converter in the backward direction. The most attractive feature of the proposed converter is that, by employing the bidirectional switch and corresponding switching modulation, it can achieve almost ZVS at turn-OFF instants under wide variations of battery voltages. Therefore, the proposed converter achieves high efficiency even during high-frequency operation. Moreover, no instantaneous reactive current flows through the circuit under wide variations of battery voltages and loads. Furthermore, the proposed bidirectional resonant converter has a high conversion ratio in both power flow directions without using a transformer that has high turns-ratio. The operating principles and characteristics of the proposed bidirectional resonant converter are presented in detail. Experimental results using a 1-kW prototype verified the feasibility and efficiency of the proposed converter.**

***Index Terms*—Bidirectional switch, high efficiency, minimized switching loss, PWM full-bridge resonant-boost converter, PWM half-bridge resonant-buck converter.**

I. Introduction

THE ability to store energy is still just beginning to impact our energy systems. Energy storage industry targets three main markets: mobility, stationary, electronic devices, which are expected to grow by 18-fold to 3082 GWh by 2035, up from the 164 GWh in 2019 [1], [2]. The energy storage units, particularly the battery units, contain a number of low-voltage battery cells. To realize the connection of the low voltage battery and high-voltage dc-bus and meanwhile maintain or improve the power quality and reliability, it is necessary to introduce bidirectional converters with high-voltage conversion ratio as a mediation module; also, it must cope with the battery voltages that vary in a wide range. Thus, designing bidirectional dc/dc converters that have high voltage gain and achieve high efficiency over a wide range of battery voltages is the subject of considerable research.

Bidirectional flyback converters are simple in structure and control, and require few power components, and are therefore suitable for use in small- and medium-sized energy storage systems (ESSs). Unfortunately, the leakage inductor of the transformer induces switching loss from the power switches and the output diode suffers from serious reverse-recovery problems; these defects degrade power conversion efficiency significantly. To alleviate the effect of leakage inductor, an active-clamp circuit has been added to the flyback converter in [4]. The active clamp circuit recycles the energy that has been stored in the leakage and magnetizing inductances of the transformer. It also maintains the voltage on the power switches at a specific voltage level. Then, a low-voltage-rated switch that has low ON-state resistance can be used, and so the converter's power conversion efficiency increases. One proposed bidirectional flyback converter [5] includes an auxiliary winding in the coupled inductor, so all power switches and diode undergo zero-current-switching (ZCS) that reduces the switching losses and voltage stresses. Another proposed parallel-input series-output converter that uses bidirectional flyback topology [6] recycles the energy stored in leakage inductance by using a dual-inductor-capacitor-diode snubber instead of traditional resistor-capacitor-diode snubbers; this change further increases efficiency. Bidirectional forward converters have been presented and adopted for small-to-medium ESSs. Forward converters are promising because they have continuous output current and its higher power density than flyback converters. In [7], the converter is developed by combining two identical two-switch forward converters through a shared transformer. The voltage stresses across the switches are clamped to the primary and secondary side voltage source. A bidirectional forward resonant converter has also been developed [8]; by transferring the power in resonant manner, it achieves ZCS for all switches. However, converters that use single-ended topology must operate with extremely high duty-ratio to achieve a very high voltage conversion ratio; such operation under an extremely high duty cycle may result in serious reverse-recovery and electromagnetic-inference problems. Another converters [9], [10] achieve a high-voltage-conversion ratio by using a transformer that has a high turns

Manuscript received September 23, 2020; revised December 8, 2020, February 6, 2021, and March 29, 2021; accepted April 24, 2021. Date of publication May 7, 2021; date of current version July 30, 2021. This work was supported by the National Research Foundation of Korea funded by the Korea Government under Grant 2021R1C1C1004276. Recommended for publication by Associate Editor J. Ye. *(Corresponding author: Minsung Kim.)*

The authors are with the Division of Electronics and Electrical Engineering, Dongguk University-Seoul, Seoul 04620, South Korea (e-mail: smi01234s@naver.com; jamilbabu70@gmail.com; mkim@dgu.ac.kr).

This article has supplementary material provided by the authors and color versions of one or more figures available at https://doi.org/10.1109/TPEL.2021.3078413.

Digital Object Identifier 10.1109/TPEL.2021.3078413

ratio, but suffers from the large leakage inductance and parasitic capacitance, which together cause high voltage spikes or high current spikes on the switching devices.

Current-fed push–pull converters can meet the requirement of high-voltage conversion ratio because they function as boost converters owing to the inherent boost inductor, so the transformer turns-ratio can be greatly reduced; as a result, leakage inductance and parasitic capacitance are reduced, so voltage or current spikes on the power devices are also reduced. Furthermore, these converters utilize transformer more efficiently than single-flyback or single-forward converters, and therefore can work at significantly higher power levels than single-flyback or single-forward converters. A bidirectional current-fed push–pull converter [11] uses a switching control strategy to obtain ZCS and zero-voltage-switching (ZVS) at turn-OFF and turn-ON of the primary side power switches. Since then, the pulsewidth modulation (PWM) plus phase shift control strategy has been applied in the converter to reduce the peak current of the switches [12]. Impulse commutation is a resonance impulse that exploits transformer leakage inductance and parallel capacitance for a short time interval. This has been used to achieve ZCS turn-OFF of the switching devices [13]. Three-phase bidirectional push–pull converters have been proposed for high-power applications [14]–[16]; these converters inherit the advantages of single-phase push–pull converters and have the higher power capability with a small number of power components, so the development cost is decreased and the system reliability is increased. However, at duty cycle $<1/3$ or $>2/3$, the circulating current increases, so these converters have limited power-transfer capability and significantly reduced efficiency. Thus, a hybrid dual-asymmetrical-PWM and PWM-plus-phase-shift switching method was introduced to increase the efficiency over a wide voltage range [17]. In another soft-switching bidirectional three-phase push–pull converter [18], the modulation of the switches clamps the voltage across the low voltage-side switches without any auxiliary power circuits. The device also achieves natural zero current commutation of low-voltage side switches and ZVS turn-ON of the high-voltage side switches so switching losses are low. However, these push–pull converters inevitably suffer from hard-switching problem at the several active switches. The seriousness of the problem increases with the switching frequency at which the circuit operates. A unidirectional resonant push–pull converter [19] may avoid hard switching by using a resonant tank and operating in resonant mode, so the switching loss is significantly reduced. The forward-operation case has since been extended to bidirectional operations by replacing the secondary diodes with active switching devices [20], but during backward power transfer, the proposed modulation is only valid at unity voltage gain. If the secondary-side switches use a symmetric duty cycle with a phase-shift technique, the power can be transferred at different voltage gains in the backward power flow direction. However, one of the main limitation of this converter is that it experiences significant turn-OFF loss when the nominal voltage gain is far from one; this loss reduces the power conversion efficiency significantly at the high switching frequency. Also, a large amount of instantaneous reactive current flows through the circuit; this current further reduces the power conversion efficiency.

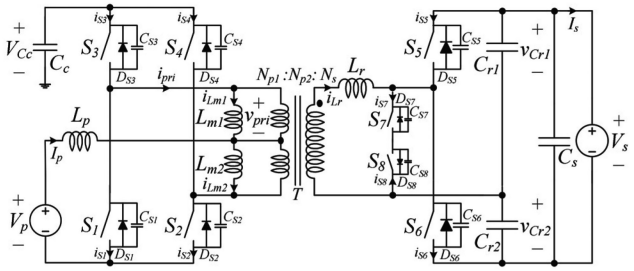

Fig. 1. Circuit diagram of the proposed converter. S_i, D_{si}, C_{si} $(i = 1, \ldots, 8)$: equivalent models of the switches; T: transformer with turns ratio N_{p1}:N_{p2}:N_s, where N_{p1} is the number of upper side primary winding turns, N_{p2} is the number of lower side primary winding turns, and N_s is the number of secondary winding turns. L_{m1}: upper side primary magnetizing inductor L_{m2}: lower side primary magnetizing inductor; L_r: resonant inductor; L_p: primary inductor; C_c: clamp capacitor; C_{r1} and C_{r2}: resonant capacitors; C_s: secondary-side capacitor; V_p: primary-side voltage source; V_s: secondary-side voltage source; v_{cr1} and v_{cr2}: voltage across C_{r1}, C_{r2}; v_{Cc}: voltage across C_c; I_p: primary current through L_p; v_{pri}: primary upper-side voltage of T; i_{Lm1}: upper-side magnetizing current; i_{Lm2}: lower-side magnetizing current; i_{Lr}: current through L_r; i_{Si} $(i = 1, \ldots, 8)$: the current through S_i $(i = 1, \ldots, 8)$; I_s: secondary current.

To overcome the problem, we propose a bidirectional push–pull resonant converter that uses a bidirectional switch on the secondary side of the transformer. With this circuit, the converter operates as a PWM current-fed push–pull resonant-boost converter in the forward direction, but as a PWM half-bridge resonant-buck converter in the backward direction. This topology and the corresponding modulation scheme realize almost ZVS at the turn-OFF instants under wide voltage variation at the low voltage side, and thereby achieves high-power conversion efficiency even with high frequency operation. Moreover, instantaneous reactive current is absent under a wide range of battery voltages and loads. Furthermore, the proposed bidirectional resonant converter accomplishes a high conversion ratio in both directions without using the transformer that has high turns-ratio. A prototype bidirectional converter was built; it operates at 48 to 72-V input voltage, 380-V output voltage, and 1-kW output power.

The rest of the article is organized in the following sections. Section II describes the circuit operations of the proposed converter. Section III analyzed its switching loss of the proposed converter and Section IV gives its controller design. Section V presented the steady-state analysis of the proposed converter and Section VI describes its design guidelines. Section VII represents the experimental setup and results. Finally, Section VIII provides the conclusion of this article.

II. Topology and System Description

The proposed converter (see Fig. 1) consists of a primary side and a secondary side. On the primary side of the transformer T, the converter exploits a current-fed push–pull circuit using two main switches S_1, S_2 and two active clamp-switches S_3, S_4, a primary inductor L_p, and a clamp capacitor C_c. On the secondary side of T, the converter employs a PWM resonant half-bridge

circuit that use two switches S_5 and S_6, and bidirectional switch S_7 and S_8, two resonant capacitors C_{r1} and C_{r2}, and a resonant inductor L_r that is composed of the leakage inductance of the transformer and an external inductor.

The proposed converter operates as a PWM push–pull resonant-boost converter in the forward direction. (S_1, S_4) and (S_2, S_3) are treated as two diagonal switch pairs, and each of which is driven by two left-aligned PWM signals that have the same duty cycle $0.5-t_{df}/T_s$ and the same dead-time t_{df}, but are 180° out of phase with each other. S_8 is turned ON when S_2 and S_3 are turned ON, whereas S_7 is turnedON when S_1 and S_4 are turned ON. After S_7 and S_8 are turned ON, they are turned OFF after $(D_s+0.5)T_s$. The proposed converter operates as a PWM half-bridge resonant-buck converter in the backward direction. S_1 and S_2 are turned OFF. S_3 and S_4 are driven by two PWM signals that have the same duty cycle $0.5-t_{db}/T_s$ and the same dead-time t_{db}, but are 180° out of phase with each other. (S_5, S_7) and (S_6, S_8) are treated as two diagonal switch pairs, each of which is driven by two left-aligned PWM signals that have the same duty cycle D_b and the same dead time t_{db}.

To analyze the steady-state operation of the proposed converter, we make four assumptions.

1) All switches $S_1, \ldots, S_8$ are ideal except for their body diodes $D_{s1}, \ldots, D_{s8}$ and output capacitors $C_{s1}, \ldots, C_{s8}$.

2) Clamp capacitor C_c and secondary-side capacitor C_s are sufficiently large that clamp capacitor voltage V_{Cc} and secondary-side voltage source V_s can be considered constant.

3) T is composed of an ideal transformer that has magnetizing inductance $L_{m1,2}$ and secondary leakage inductance. L_r is the series connection of the transformer leakage inductance and an external inductance.

4) The resonant capacitors C_{r1} and C_{r2} are identical, with capacitances $C_{r1} + C_{r2} = C_r$.

In forward direction, the operation of the proposed converter can be divided into four modes (see Fig. 2) that have the corresponding waveforms (see Fig. 3). The converter operated symmetrically, so we describe only the modes during the first half of the switching period.

A. Analysis of PWM Push–Pull Resonant-Boost Converter

Mode 1 [t_0, t_1]: At time t_0, the voltage across S_8 is zero, and the current begins to flow through D_{S8}. Thus, S_8 is turned ON with ZVS. During this interval, nV_{Cc} increases the current flowing through the resonant inductor linearly. The state equation of this equivalent circuit is

$$L_r \frac{di_{Lr}(t)}{dt} = nV_{Cc} \tag{1}$$

with the initial condition $i_{Lr}(t_0) = 0$. Solving (1) for $i_{Lr}(t)$ yields

$$i_{Lr}(t) = \frac{nV_{Cc}}{L_r}(t - t_0). \tag{2}$$

Meanwhile, the resonant capacitor voltage stays at

$$v_{cr1}(t) = \frac{V_s}{2} - \Delta V_{cr}. \tag{3}$$

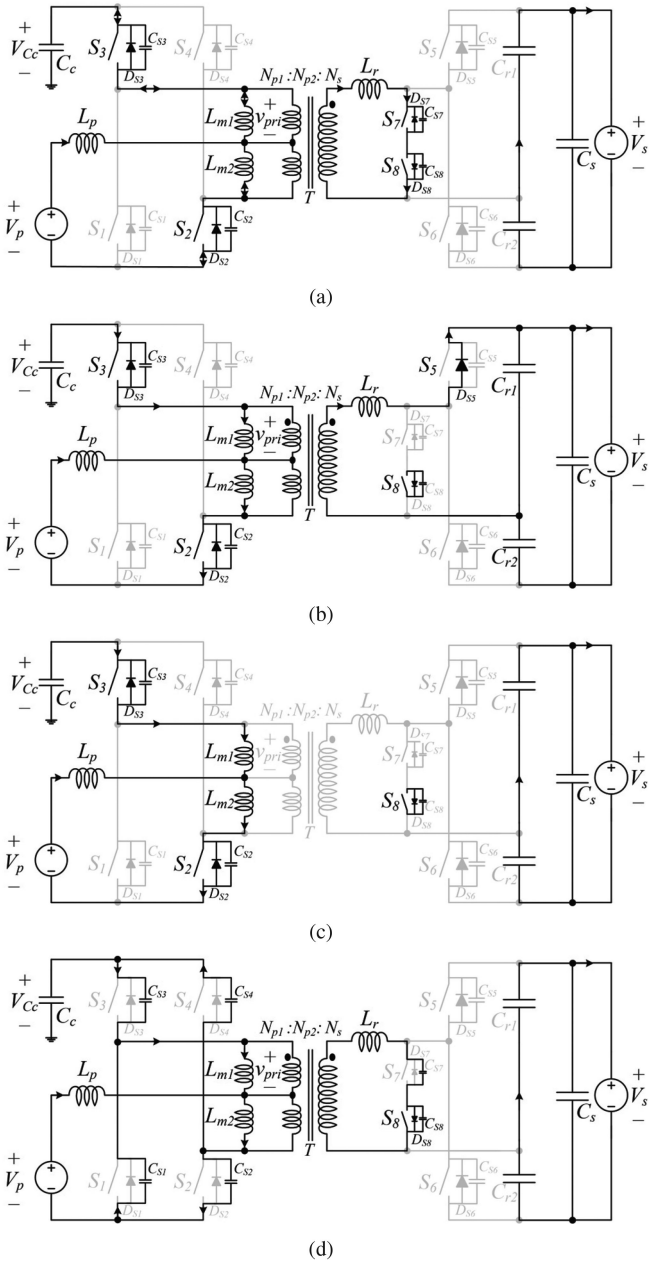

Fig. 2. Equivalent circuits of the proposed converter operating in forward mode. (a) Mode 1. (b) Mode 2. (c) Mode 3. (d) Mode 4.

The operation point moves along the trajectory curve from A_1 to B_1 (see Fig. 4).

Mode 2 [t_1, t_2]: At time t_1, S_7 is turned OFF with almost ZVS, because v_{ds7} is equal to $V_s/2 - \Delta V_{Cr}$. The current on the primary side then flows through D_{S5}. During this interval, the active clamp capacitor, the resonant inductor, and the resonant capacitor form an equivalent closed circuit, and the resonant inductor current goes to zero following the sinusoidal waveform. The state equation that corrresponds to this equivalent circuit can be written as

$$L_r \frac{di_{Lr}(t)}{dt} = nV_{Cc} - v_{cr1}(t) \tag{4}$$

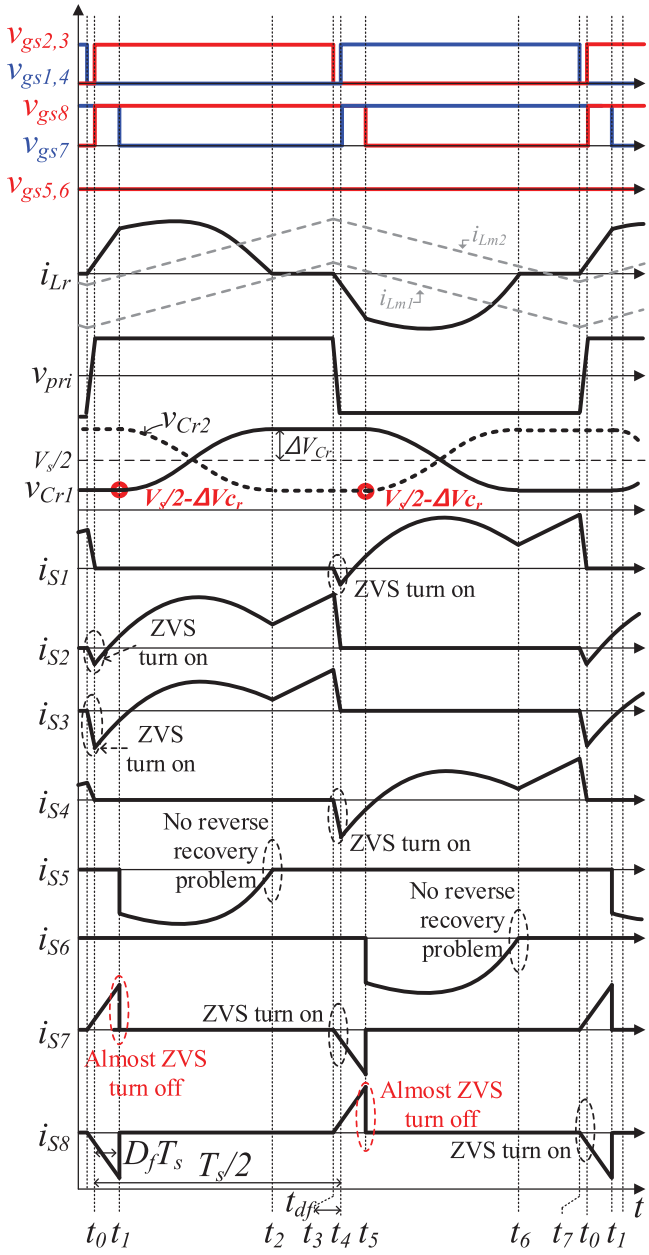

Fig. 3. Theoretical waveforms of the proposed converter operating in forward mode. $v_{gs'i'}$ is the gate-source voltage of the ith switch.

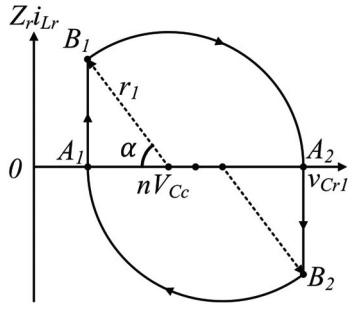

Fig. 4. State-plane trajectory of the proposed converter operating in forward mode.

$$i_{Lr}(t) = C_r \frac{dv_{cr1}(t)}{dt} \tag{5}$$

with $i_{Lr}(t_1) = \frac{r_1}{Z_r}\sin\alpha$ and $v_{cr1}(t_1)=nV_{Cc} - r_1\cos\alpha$, where $\alpha = \sin^{-1}(\frac{nV_{Cc}Z_r}{L_r r_1}(t_1 - t_0))$. Solving (4) and (5) yields

$$i_{Lr}(t) = \frac{r_1}{Z_r}\sin[\alpha + \omega_r(t - t_1)] \tag{6}$$

$$v_{cr1}(t) = nV_{Cc} - r_1\cos[\alpha + \omega_r(t - t_1)] \tag{7}$$

where $r_1 = \frac{V_s}{2} + \Delta V_{Cr} - nV_{Cc}$ is the radius of the circular path that has a center at $(nV_{Cc}, 0)$ (see Fig. 4). The operating point moves along the trajectory curve from B_1 to A_2 (see Fig. 4), and the resonant angular frequency ω_r and the characteristic impedance Z_r are obtained as

$$\omega_r = \frac{1}{\sqrt{L_r C_r}}, \quad Z_r = \sqrt{\frac{L_r}{C_r}}. \tag{8}$$

Mode 3 [t_2, t_3]: At time t_2, i_{Lr} is zero and v_{Cr1} is at its maximum. i_{s2} and i_{s3} are increased linearly because of i_{Lm1}, i_{Lm2}, and i_{Lr}. At t_2, D_{S5} is turned OFF with no reverse recovery problem. At this time, the trajectory path stays at A_2 (see Fig. 4).

Mode 4 [t_3, t_4]: At time t_3, S_2 and S_3 are turned OFF. Then, the circuit enters the dead-time zone. During this time, i_{Lm1} and i_{Lr} appear as the current source to the primary side, and charge C_{S2} and C_{S3} while discharging C_{S1} and C_{S4}. Thus, S_1 and S_4 are turned ON with ZVS. The trajectory path still stays at A_2 during this interval.

B. Analysis of PWM Half-Bridge Resonant-Buck Converter

In backward direction, the operation of the proposed converter can also be divided into four modes (see Fig. 5), which have corresponding waveforms (see Fig. 6). The converter is operated symmetrically, so again we describe only the modes during the first half of the switching period.

Mode 1 [t_0, t_1]: At time t_0, the voltage across S_6 is zero and i_{Lr} starts to flow through D_{S6}. Thus, S_6 is turned ON with ZVS. During this interval, the primary-side voltage of T is equal to nV_{Cc} and the primary side current i_{pri} begins to flow through D_{S1} and D_{S4}. The state equation that corresponds to this equivalent circuit is

$$L_r \frac{di_{Lr}(t)}{dt} = nV_{Cc} - v_{Cr2}(t) \tag{9}$$

$$i_{Lr}(t) = C_r \frac{dv_{Cr2}(t)}{dt} \tag{10}$$

with $i_{Lr}(t_0) = 0$ and $v_{Cr2}(t_0) = V_s/2 + \Delta V_{Cr}$.

Solving (9) and (10) yields

$$i_{Lr}(t) = -\frac{r_2}{Z_r}\sin[\omega_r(t - t_0)] \tag{11}$$

$$v_{Cr2}(t) = nV_{Cc} - r_2\cos[\omega_r(t - t_0)] \tag{12}$$

where $r_2 = \frac{V_s}{2} + \Delta V_{Cr} - nV_{Cc}$ is the radius of circular path with center at $(nV_{Cc}, 0)$ (see Fig. 7). Here the operating point moves along the trajectory curve from A_2 to B_2 (see Fig. 7).

Mode 2 [t_1, t_2]: At time t_1, S_6 is turned OFF with almost ZVS because v_{ds6} is equal to $V_s/2 - \Delta V_{Cr}$. The current flows

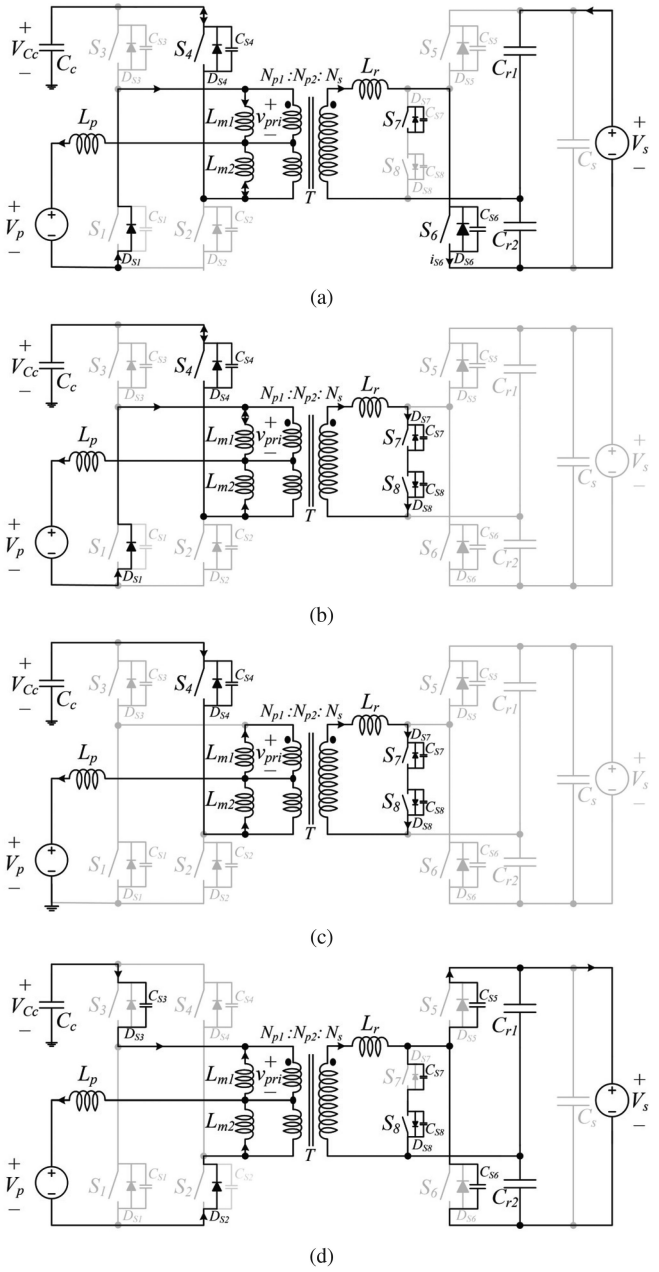

Fig. 5. Equivalent circuits of the proposed converter operating in backward mode. (a) Mode 1. (b) Mode 2. (c) Mode 3. (d) Mode 4.

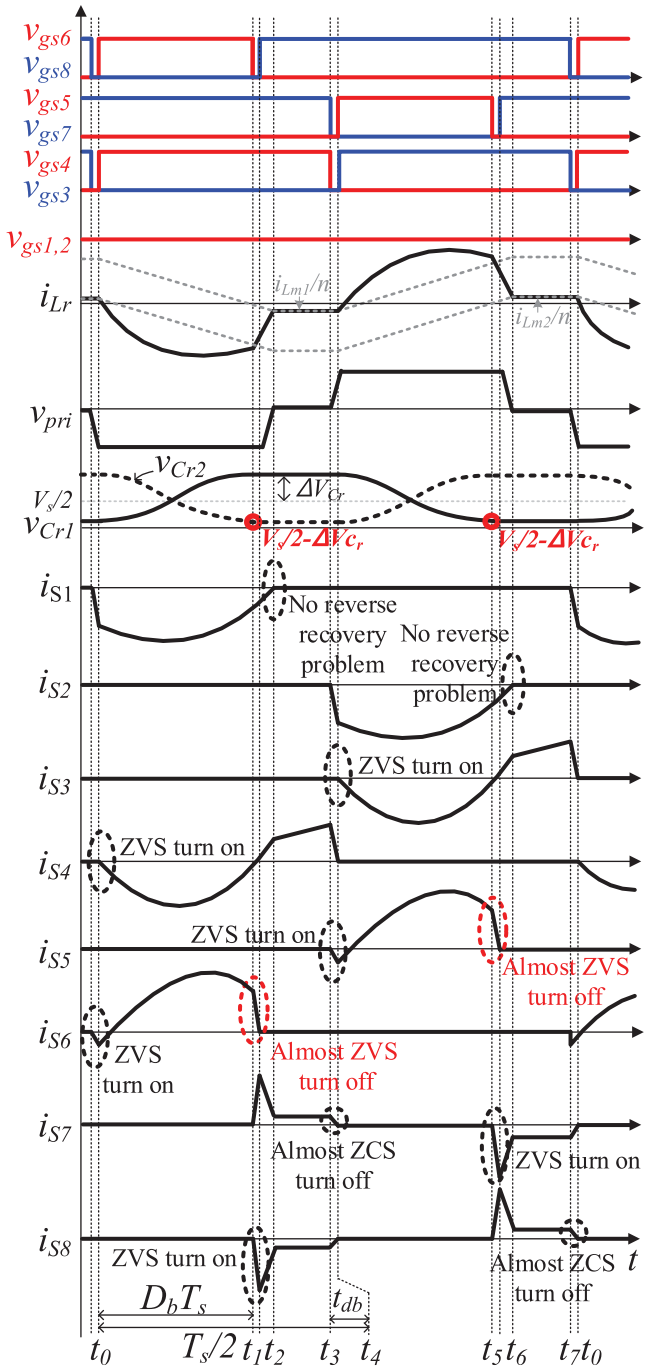

Fig. 6. Theoretical waveforms of the proposed converter operating in backward mode.

through D_{S8}. After the given dead time, S_8 is then turned ON with ZVS. During this mode, only the primary side voltage nV_{Cc} is applied to L_r and the primary side current i_{pri} flow through D_{S1} and S_4. Thus, i_{Lr} quickly goes to zero. In this mode, the state equation of the circuit can be written as

$$L_r \frac{di_{Lr}(t)}{dt} = nV_{Cc} \tag{13}$$

with $i_{Lr}(t_1) = -\frac{r_2}{Z_r}\sin(\pi-\beta)$, $\beta = \cos^{-1}\left(\frac{\Delta V_{Cr} - V_s/2 + nV_{Cc}}{r_2}\right)$. Solving (13) yields

$$i_{Lr}(t) = \frac{nV_{Cc}}{L_r}(t-t_1) - \frac{r_2}{Z_r}\sin(\pi-\beta). \tag{14}$$

Meanwhile, the resonant capacitor voltage stays at

$$v_{cr2}(t) = \frac{V_s}{2} - \Delta V_{Cr}. \tag{15}$$

The operating point moves along the trajectory curve from B_2 to A_1 (see Fig. 7).

Mode 3 [t_2, t_3]: At time t_2, i_{Lr} and v_{Cr2} is at its minimum value. During this interval, the current that flows through S_7 and D_{S8} is the magnetizing current i_{Lm1}/n. By selecting L_{m1}

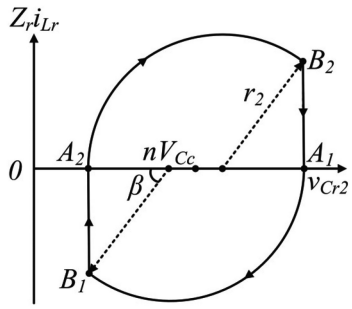

Fig. 7. State-plane trajectory of the proposed converter operating in backward mode.

to make i_{S7} and i_{S8} small, S_7 can be turned OFF with almost ZCS at time t_3. Here, the trajectory path stays at point A_1 (see Fig. 7).

Mode 4 [t_3, t_4]: At time t_3, the converter enters the dead-time zone. During this mode, i_{Lm1}/n acts as the current source to the primary side. This current discharges C_{S5} and C_{S7} and charges C_{S6}. When C_{S5} is completely discharged, the voltage across S_5 becomes zero and i_{Lm1}/n flows through D_{S5}. Therefore, at time t_4, S_5 is turned ON with ZVS. The trajectory path remains at point A_1 during the interval.

III. Switching Loss Analysis

In the proposed converter, $v_{Cr1} = V_s/2 - \Delta V_{Cr}$ is applied to S_7 and S_8 at turn-OFF instant in forward operation, $v_{Cr2} = V_s/2 - \Delta V_{Cr}$ is applied to S_5 and S_6 at turn-OFF instant in backward operation. The turn-OFF voltage in the proposed converter decreases by a large extent compared to that in [20], whereas in the converter in [20], hard-switching turn OFF occurs at secondary side. Fig. 8 describes that the corresponding dissipated power at S_7 and S_6 decreases in forward direction and in backward direction, respectively. The next sections will evaluate the switching losses and conduction losses of the converters.

A. Switching Losses

The total switching losses $P_{\rm sw}$ can be calculated as

$$P_{sw} = \sum P_{on,S'i'} + \sum P_{off,S'i'} \tag{16}$$

where $P_{on,S'i'}$ is the turn-ON loss of the ith switch and $P_{off,S'i'}$ is the turn-OFF loss of the ith switch. The proposed converter can achieve ZVS turn ON from the all of switching, so we can ignore $P_{on,S'i'}$, which is virtually zero.

$P_{off,S'i'}$ can be calculated as

$$P_{off,S'i'} = \frac{1}{2} V_{off,S'i'} \cdot |I_{off,S'i'}| \cdot \frac{t_{off,S'i'}}{T_s}. \tag{17}$$

$P_{off,S'i'}$ can be used to obtain the total switching losses in both power flow directions as follows.

In forward mode

$$P_{sw} = \sum P_{off,S'i'} = P_{off,S1,2} + P_{off,S3,4} + P_{off,S7,8}$$
$$= 2(P_{off,S2} + P_{off,S3} + P_{off,S7})$$

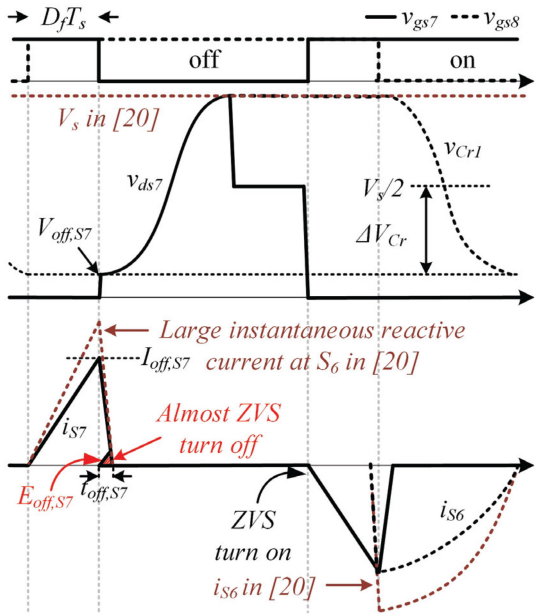

(a)

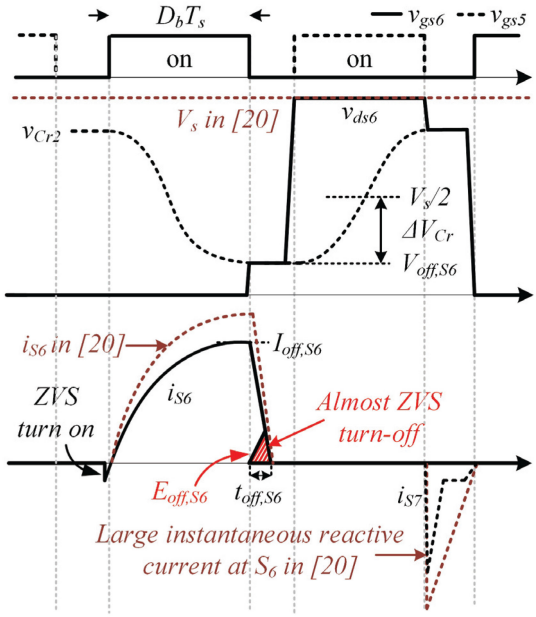

(b)

Fig. 8. Zoom-in waveforms of the switching loss in the proposed converter at the turn-OFF instant. $E_{off,S'i'}$ is the dissipated power of ith switch at the turn-OFF instant. $V_{off,S'i'}$ is the voltage across the ith switch at turn-OFF instant. $I_{off,S'i'}$ is the current flowing through the ith switch at turn-OFF instant. $V_{ds'i'}$ is the drain-source voltage across the ith switch. $t_{off,S'i'}$ is the fall time of the ith switch. (a) At S_7 in forward direction. (b) At S_6 in backward direction.

$$= 2V_{off,S2} \cdot \left| \frac{1}{2} I_p(t_3) + i_{Lm2}(t_3) \right| \cdot \frac{t_{off,S2}}{2T_s} + 2V_{off,S3}$$
$$\cdot \left| -\frac{1}{2} I_p(t_3) + i_{Lm1}(t_3) \right| \cdot \frac{t_{off,S3}}{2T_s} + 2V_{off,S7} \cdot |i_{Lr}(t_1)|$$
$$\cdot \frac{t_{off,S7}}{2T_s}$$

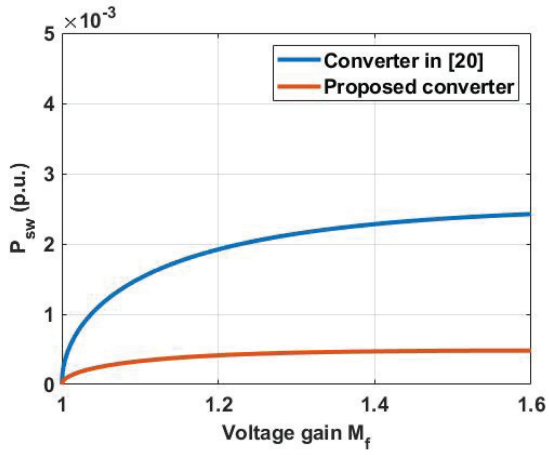

(a)

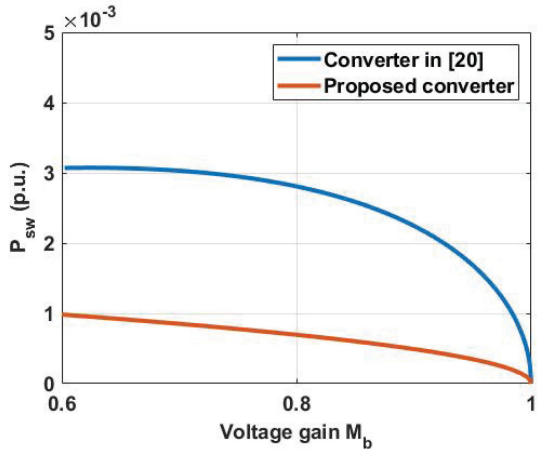

(b)

Fig. 9. Turn-OFF switching loss values of the proposed converter and the conventional converter in [20] at rated power subject to input voltage variations. (a) Per-unit $P_{\rm sw}$ in forward direction. (b) Per-unit $P_{\rm sw}$ in backward direction.

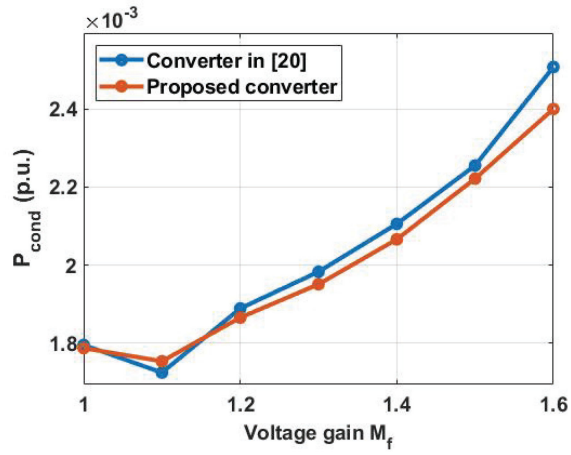

(a)

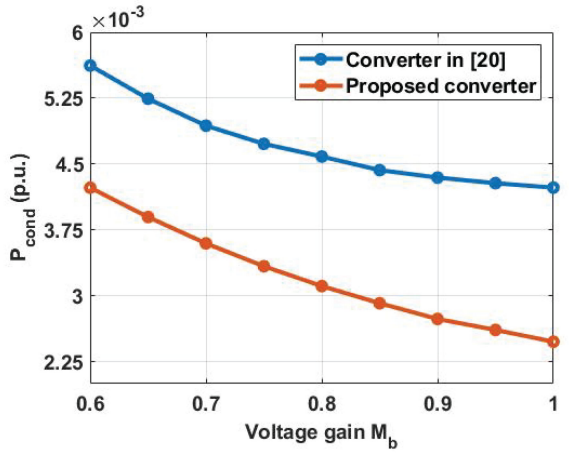

(b)

Fig. 10. Conduction losses of the proposed converter and the conventional converter in [20] at rated power subject to input voltage variations. (a) Per-unit $P_{\rm cond}$ in forward direction. (b) Per-unit $P_{\rm cond}$ in backward direction.

$$= V_{Cc} \cdot \left| \frac{P_s}{2V_p} + \frac{V_{Cc}}{2L_{m1}} \right| \cdot \frac{t_{off,S2}}{T_s} + V_{Cc} \cdot \left| -\frac{P_s}{2V_p} + \frac{V_{Cc}}{2L_{m2}} \right| \cdot \frac{t_{off,S3}}{T_s} + \left| \frac{V_s}{2} - \Delta V_{C_r} \right| \cdot \frac{nV_{Cc}}{L_r} \cdot \frac{t_{off,S7}}{T_s}. \quad (18)$$

In backward mode

$$P_{sw} = \sum P_{off,S'i'} = P_{off,S3,4} + P_{off,S5,6}$$

$$= 2(P_{off,S4} + P_{off,S6})$$

$$= 2V_{off,S4} \cdot |I_p(t_3)| \cdot \frac{t_{off,S4}}{2T_s} + 2V_{off,S6} \cdot |i_{Lr}(t_1)| \cdot \frac{t_{off,S6}}{2T_s}$$

$$= V_{Cc} \cdot \left| \frac{P_s}{V_p} \right| \cdot \frac{t_{off,S4}}{T_s} + \left(\frac{V_s}{2} - \Delta V_{C_r} \right) \cdot \left| \frac{r_2}{Z_r} \sin[w_r(t_1 - t_0)] \right| \cdot \frac{t_{off,S6}}{T_s}. \quad (19)$$

Fig. 9 depicts the per-unit switching loss values of the proposed converter and the conventional converter [20]. Per-unit $P_{\rm sw}$ is defined as $P_{sw}/|P_s|$ with the output power P_s and is calculated using (18) and (19). Calculated switching losses are much smaller in the proposed converter than in the converter in [20].

B. Conduction Losses

The conduction losses are estimated for the interval in which the active components are conducting. The total conduction losses $P_{\rm cond}$ can be calculated as

$$P_{\rm cond} = \sum P_{cond,S'i'} + \sum P_{cond,D'j'} \quad (20)$$

where $P_{cond,S'i'}$ is the conduction loss when the ith switch is ON and $P_{cond,D'j'}$ is the conduction loss when the ith switch is OFF.

The conduction loss of the each MOSFET switch while it is turned ON can be calculated as

$$P_{cond,S'i'} = I^2{}_{S'i'} R_{ds'i'} \quad (21)$$

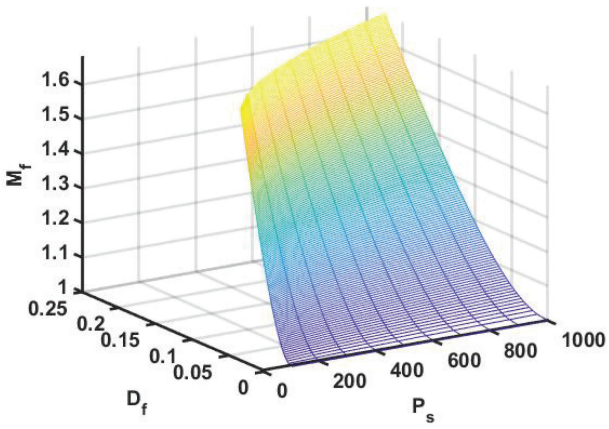

(a)

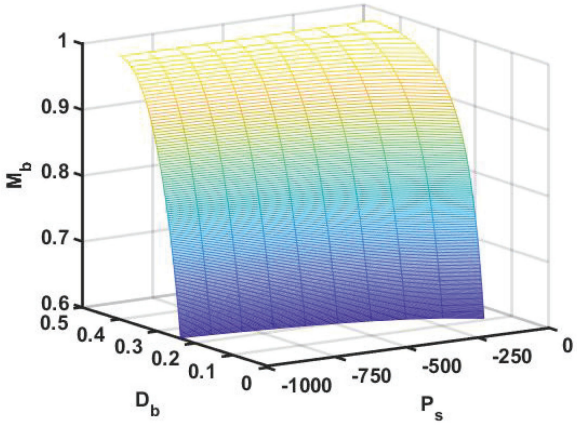

(b)

Fig. 11. Voltage gain surfaces of the proposed converter. (a) M_f. (b) M_b.

where $I_{S'i'}$ is the root-mean-square (rms) current flowing through the ith switch and $R_{ds'i'}$ is the drain to source ON-state resistance of the ith switch.

The conduction loss of the each MOSFET switch while the switch is turned OFF can be calculated as

$$P_{cond,D'j'} = V_{D'j'} I_{D'j'} \tag{22}$$

where $V_{D'j'}$ is the voltage of the each switch and $I_{D'j'}$ is the average current flowing through the jth switch's internal diode.

Fig. 10 depicts the per-unit conduction loss values of the proposed converter and the conventional converter [20]. Per-unit P_{cond} is defined as $P_{\text{cond}}/|P_s|$ and can be calculated using (20)−(22). Note that we have used different values of $V_{D'j'}$ on the primary-side switches and constant value of $V_{D'j'}$ on the secondary-side switches in (22), because only primary-side switches provide the *I–V* curve of their reverse diodes. The proposed converter have the additional conduction loss due to the use of bidirectional switch, but does not experience instantaneous reactive current flow irrespective of wide variations of input voltages, whereas the converter in [20] suffers from larger instantaneous reactive current as the voltage gain increases. Therefore, calculated conduction losses in forward direction are

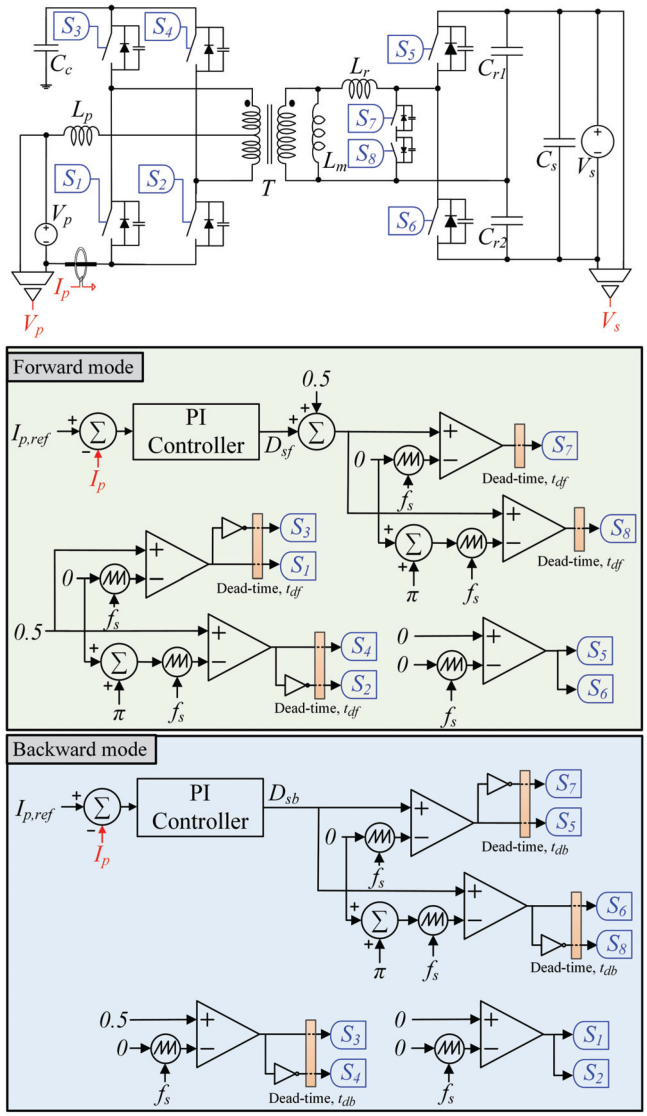

Fig. 12. Configuration of the control scheme for the proposed bidirectional converter. $I_{p,ref}$ is the reference primary current. PI controller stands for proportional-integral controller.

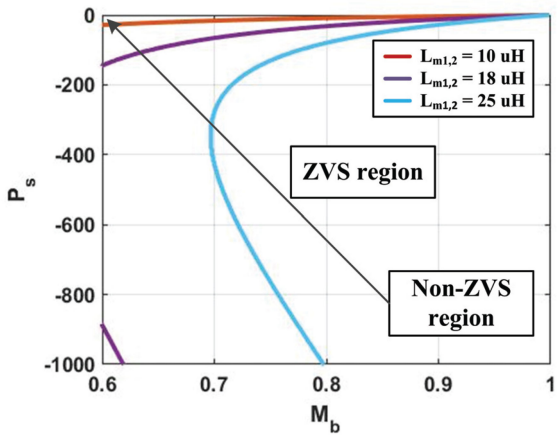

Fig. 13. ZVS region in backward direction with respect to $L_{m1,2}$, P_s, and M_b.

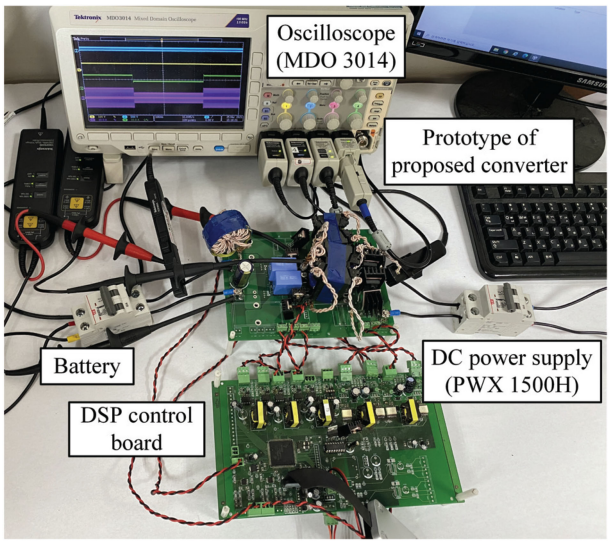

Fig. 14. Experimental setup of the proposed converter system.

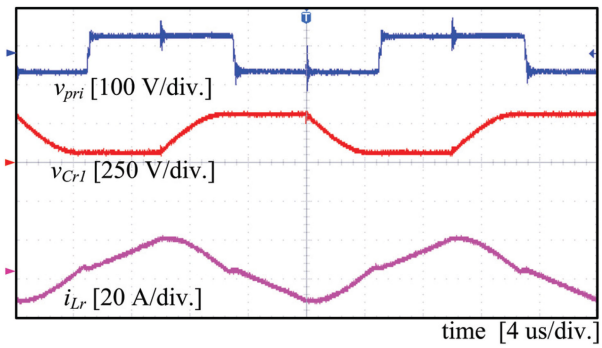

(a)

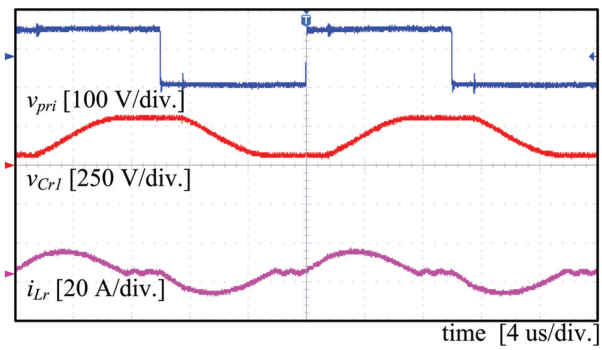

(b)

Fig. 15. Experimental waveforms of v_{pri}, v_{Cr1}, and i_{Lr} in forward mode at full load. (a) $V_p = 48$ V. (b) $V_p = 72$ V.

slightly smaller in the proposed converter than in the converter in [20] [see Fig. 10(a)]. In backward direction, the proposed converter does not use the body diodes of the secondary-side switches in power transfer, but the converter in [20] uses the body diodes of the secondary-side switches. As a result, calculated conduction losses in backward direction are much smaller in the proposed converter than in the converter in [20] [see Fig. 10(b)].

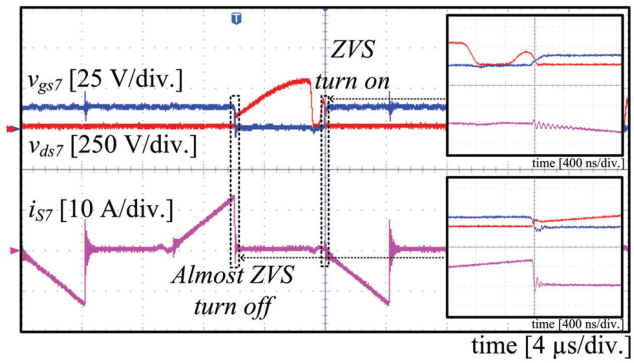

(a)

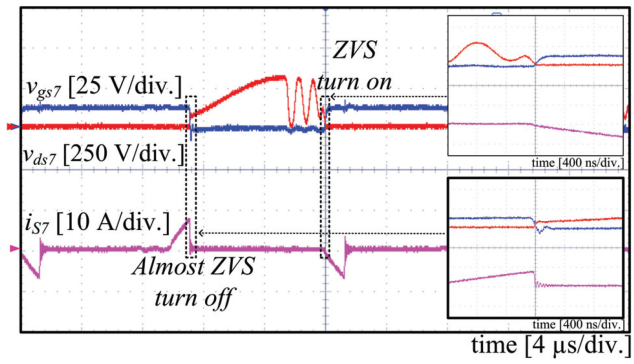

(b)

Fig. 16. Experimental waveforms of v_{gs7}, v_{ds7}, and i_{S7} in forward mode at full load. (a) $V_p = 48$ V. (b) $V_p = 72$ V.

IV. Steady-State Analysis of the Proposed Converter

A. Voltage Gain of PWM Push–Pull Resonant-Boost Converter

During the switching period T_s, the voltage-second balance law of L can be written as

$$V_p \cdot 0.5T_s + (V_p - V_{Cc}) \cdot 0.5T_s = 0. \tag{23}$$

Rearranging (23) gives

$$V_{Cc} = 2V_p. \tag{24}$$

To calculate the voltage gain of the PWM push–pull resonant converter, we first compute the resonant-capacitor voltage ripple ΔV_{Cr}. Due to symmetric operation of the voltage-doubler during the steady state, the average value of the resonant inductor current is twice the average value of the secondary source current I_s. So I_s can then be determined as

$$I_s = \frac{P_s}{V_s} = \frac{2}{T_s}\left[\int_{t_1}^{t_2} \frac{r_1}{2Z_r}\sin[\alpha + \omega_r(\tau - t_1)]\,d\tau\right]$$
$$= \frac{1}{T_s Z_r \omega_r}[r_1(1+\cos\alpha)] = \frac{2\Delta V_{Cr}}{T_s Z_r \omega_r} = \frac{2C_r \Delta V_{Cr}}{T_s}. \tag{25}$$

Rearranging (25) for ΔV_{Cr} yields

$$\Delta V_{Cr} = \frac{P_s T_s}{2V_s C_r} \tag{26}$$

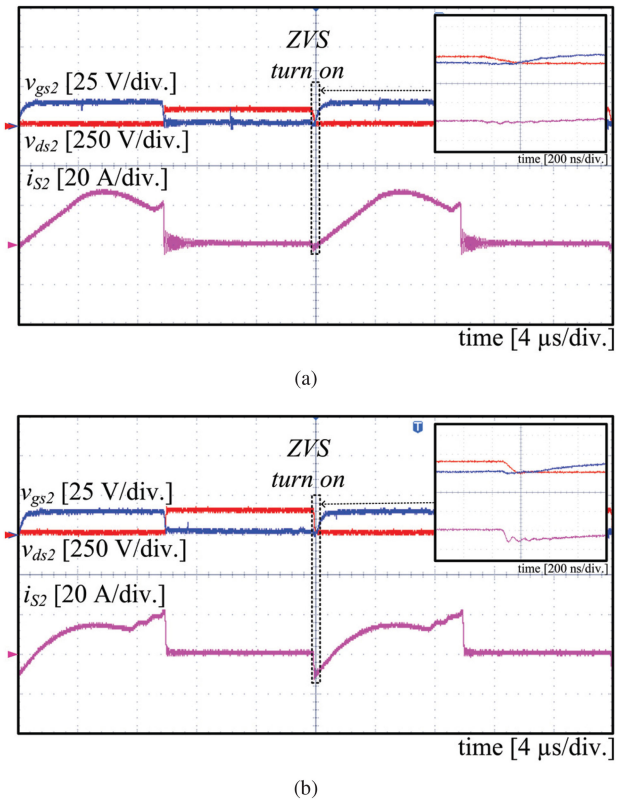

Fig. 17. Experimental waveforms of v_{gs2}, v_{ds2}, and i_{S2} in forward mode at full load. (a) $V_p = 48$ V. (b) $V_p = 72$ V.

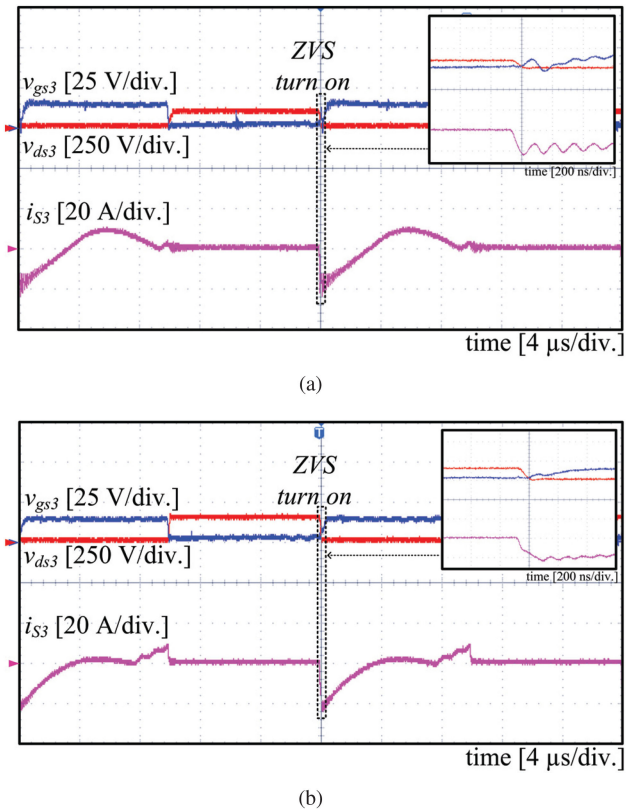

Fig. 18. Experimental waveforms of v_{gs3}, v_{ds3}, and i_{S3} in forward mode at full load. (a) $V_p = 48$ V. (b) $V_p = 72$ V.

and applying $(t_1 - t_0) = D_f T_s$ (see Fig. 3) to (2) and from (3), we can calculate $i_{Lr}(t)$ and $v_{Cr1}(t)$ at t_1 as

$$i_{Lr}(t_1) = \frac{nV_{Cc}}{L_r} D_f T_s \tag{27}$$

$$v_{Cr1}(t_1) = \frac{V_s}{2} - \Delta V_{Cr}. \tag{28}$$

As shown in Fig. 4, the circle equation with center $(nV_{Cc}, 0)$ and radius r_1 is described as

$$(v_{Cr1}(t) - nV_{Cc})^2 + (Z_r i_{Lr}(t))^2 = r_1^2. \tag{29}$$

Substituting (27) and (28) into (29) yields

$$D_f = \frac{2M_f}{V_s} \sqrt{\frac{L_r P_s}{T_s} \left(1 - \frac{1}{M_f}\right)} \tag{30}$$

where $M_f = \frac{V_s}{2nV_{Cc}}$ is the voltage gain of the PWM push–pull resonant–boost converter.

A three-dimensional graph of M_f with respect to D_f and P_s is shown in Fig. 11(a).

B. Voltage Gain of PWM Half-Bridge Resonant-Buck Converter

By using the same method as that used to derive the voltage gain of the PWM push–pull resonant-boost converter, we have

$$\begin{aligned} I_s = \frac{P_s}{V_s} &= \frac{2}{T_s} \left[\int_{t_0}^{t_1} -\frac{r_2}{2Z_r} \sin[\omega_r(\tau - t_0)]\, d\tau \right] \\ &= \frac{1}{T_s Z_r \omega_r} (r_2(\cos[\omega_r(t_1 - t_0)] - 1)) \\ &= -\frac{2\Delta V_{Cr}}{T_s Z_r \omega_r} = -\frac{2C_r \Delta V_{Cr}}{T_s}. \end{aligned} \tag{31}$$

Rearranging (31) for ΔV_{Cr} yields

$$\Delta V_{Cr} = -\frac{P_s T_s}{2V_s C_r} \tag{32}$$

and applying $(t_1 - t_0) = D_b T_s$ (see Fig. 7) to (14) and from (15), we can calculate $i_{Lr}(t)$ and $v_{Cr2}(t)$ at t_1 as

$$i_{Lr}(t_1) = -\frac{r_2}{Z_r} \sin[\omega_r D_b T_s] \tag{33}$$

$$v_{Cr2}(t_1) = \frac{V_s}{2} - \Delta v_{Cr}. \tag{34}$$

As shown in Fig. 7, the circle equation with center $(nV_{Cc}, 0)$ and radius r_2 is described as

$$(v_{Cr2}(t) - nV_{Cc})^2 + (Z_r i_{Lr}(t))^2 = r_2^2. \tag{35}$$

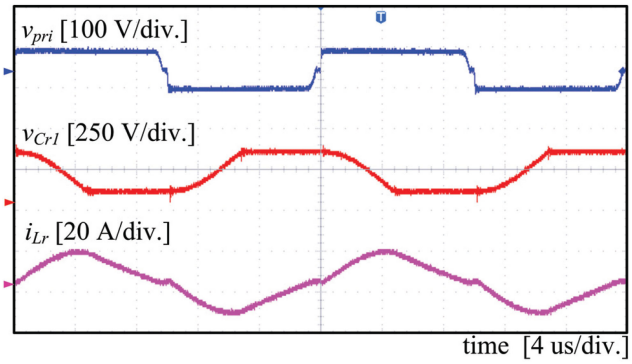

(a)

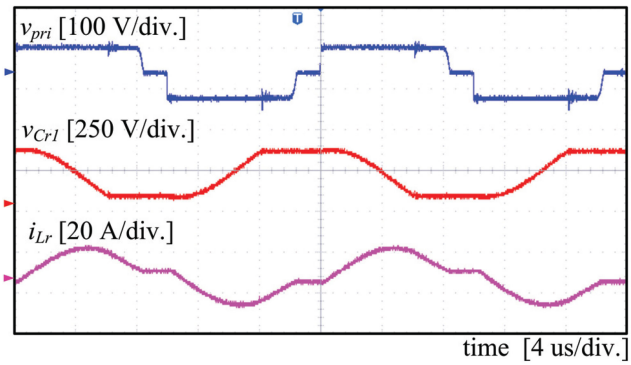

(b)

Fig. 19. Experimental waveforms of v_{pri}, v_{Cr1}, and i_{Lr} in backward mode at full load. (a) $V_p = 48$ V. (b) $V_p = 72$ V.

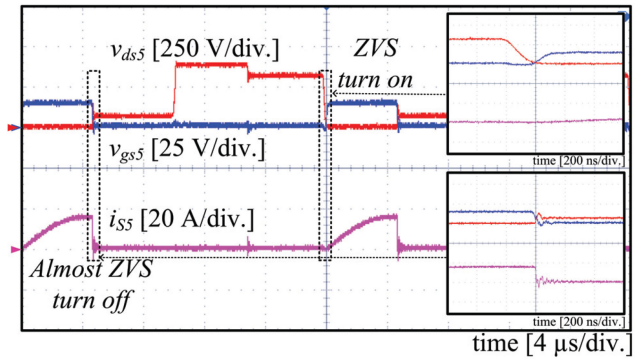

(a)

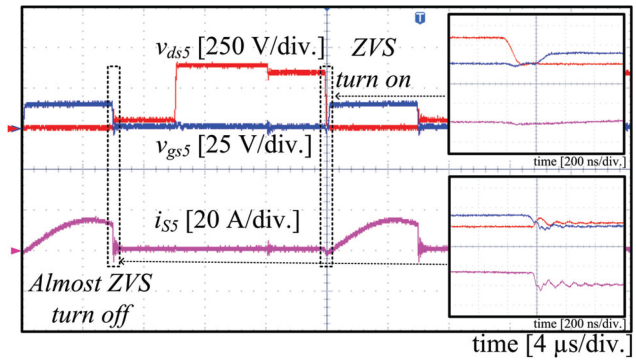

(b)

Fig. 20. Experimental waveforms of v_{gs5}, v_{ds5}, and i_{S5} in backward mode at full load. (a) $V_p = 48$ V. (b) $V_p = 72$ V.

Substituting (33) and (34) into (35) yields

$$D_b = \frac{1}{\omega_r T_s} \cos^{-1}\left(\frac{4n^2 C_r V_{Cc}^2 (1 - M_b) + M_b^2 P_s T_s}{4n^2 C_r V_{Cc}^2 (1 - M_b) - M_b^2 P_s T_s}\right) \quad (36)$$

where $M_b = \frac{2nV_{Cc}}{V_s}$ is the voltage gain of the half-bridge resonant-buck converter.

A three-dimensional graph of M_b with respect to D_b and P_s is shown in Fig. 11(b).

V. Controller Design

We developed a bidirectional control strategy for the proposed bidirectional converter as given in Fig. 12. In the forward power transfer, the current controller first determines the high-voltage side current error first by subtracting I_s from $I_{s,ref}$. It is then supplied as an input to the proportional-integral (PI) current controller. The controller output is added with 0.5 and the resulting value is then used to control the bidirectional switch S_7 and S_8. The fixed duty-ratio 0.5 is applied to the primary-side switches S_1–S_4. The secondary-side switches S_5 and S_6 are set to be turned OFF. In the backward power transfer, the current controller first determines the low-voltage side current error first by subtracting I_p from $I_{p,ref}$. The error is then supplied as an input to the PI controller. The controller output is then utilized in controlling the secondary-side switches S_5–S_8. The fixed duty-ratio 0.5 is applied to the primary-side switches S_3 and S_4. The primary-side switches S_1 and S_2 are set to be turned OFF.

VI. Design Guideline

A. Selection of Transformer Turns Ratio

The turns ratio of transformer can be determined from the voltage gain of the proposed converter. It then follows that

$$n \le \frac{V_s}{2V_{p\_\max}} \quad (37)$$

where V_{p_max} is the maximum value of the primary source voltage.

B. Magnetizing Inductance

We define t_{df} and t_{db} as the dead times for the switches in forward and backward directions. Since the dead times are very short compared to the switching period, i_{Lm1} and i_{Lm2} essentially serves as constant current sources I_{Lm1} and I_{Lm2}. In the forward mode, i_{Lm1} and i_{Lr} discharge the parasitic capacitor C_{S1}, C_{S4} and charge the parasitic capacitor C_{S2}, C_{S3} during the dead time at the end of first half switching period. To achieve ZVS, i_{Lm1} and i_{Lr} must fully discharge C_{S1} and C_{S4}. Here, ZVS condition for S_1 is more strict than the ZVS condition for

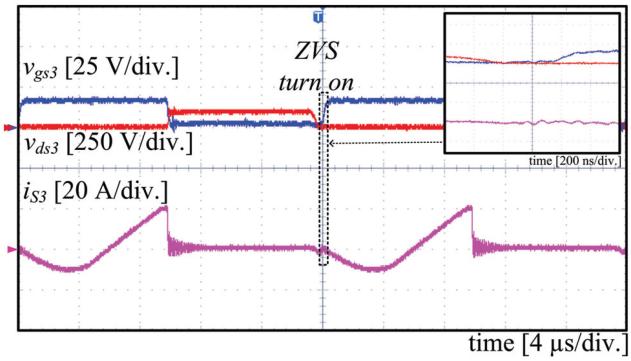

(a)

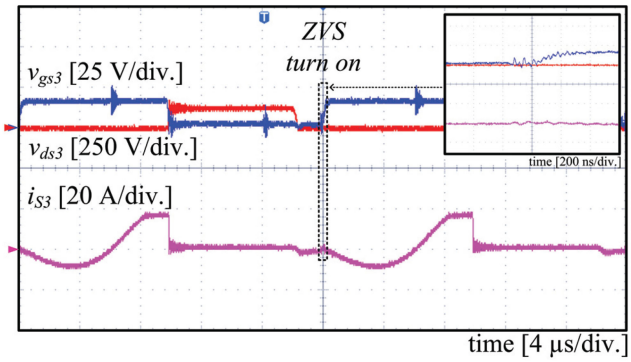

(b)

Fig. 21. Experimental waveforms of v_{gs3}, v_{ds3}, and i_{S3} in backward mode at full load. (a) $V_p = 48$ V. (b) $V_p = 72$ V.

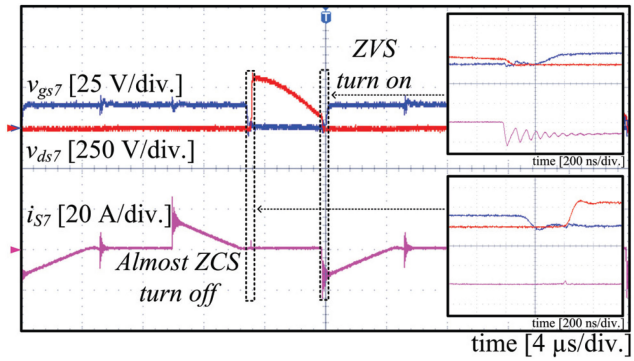

(a)

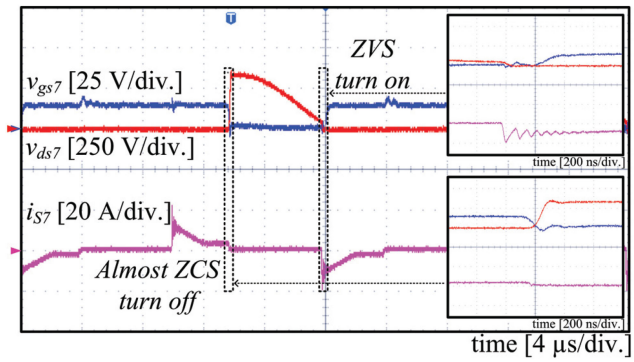

(b)

Fig. 22. Experimental waveforms of v_{gs7}, v_{ds7}, and i_{S7} in backward mode at full load. (a) $V_p = 48$ V. (b) $V_p = 72$ V.

S_4. Thus, we use

$$V_{Cc}C_{S1} < \left| \int_0^{t_{df}} \left[i_{Lm1}(\tau) + n i_{Lr}(\tau) \right] d\tau \right| = I_{Lm1} t_{df} + n \int_0^{t_{df}} \frac{n V_{Cc}}{L_r} \tau d\tau = I_{Lm1} t_{df} + \frac{n^2 V_{Cc}}{2L_r} t_{df}^2. \quad (38)$$

Substituting $I_{Lm1} = \frac{V_{Cc}T_s}{8L_{m1}} + \frac{1}{2}I_p = \frac{V_{Cc}T_s}{8L_{m1}} + \frac{P_s}{2V_p}$ into (38) and rearranging it with respect to L_{m2}, we have

$$L_{m1} < \frac{V_{Cc}T_s t_{df}}{8V_{Cc}C_{S1} - \frac{4n^2 V_{Cc} t_{df}^2}{L_r} - \frac{4P_s t_{df}}{V_p}}. \quad (39)$$

Solving (39), we obtain simple ZVS region in forward direction according to the value of $L_{m1,2}$. Given $L_{m1,2}$, the primary-side switches can achieve ZVS in forward direction except for the light load.

In the backward mode, i_{Lm1}/n discharges C_{S5}, C_{S7} and charges C_{S6} during the dead time. To achieve ZVS, i_{Lm1}/n must fully discharge C_{S5}. Then, the condition to achieve ZVS in the backward mode becomes

$$(V_s/2 + \Delta V_{C_r})(C_{S5} + C_{S6} + C_{S7}) < \left| \int_0^{t_{db}} \left[\frac{1}{n} i_{Lm1}(\tau) \right] d\tau \right| = \frac{1}{n} I_{Lm1} t_{db}. \quad (40)$$

Substituting $I_{Lm1} = \frac{V_{Cc}(D_b + D_{bz})T_s}{4L_{m1}} - \frac{1}{2}I_p = \frac{V_{Cc}(D_b + D_{bz})T_s}{4L_{m1}} - \frac{P_s}{2V_p}$ into (40), we have

$$L_{m1} < \frac{V_{Cc}(D_b + D_{bz})T_s t_{db}}{4n(V_s/2 + \Delta V_{C_r})(C_{S5} + C_{S6} + C_{S7}) + \frac{2P_s t_{db}}{V_p}}. \quad (41)$$

Here, falling duty-ratio D_{bz} is

$$D_{bz} = \frac{t_2 - t_1}{T_s} = \frac{L_r}{nV_{Cc}T_s} \frac{r_2}{Z_r} \sin[w_r(t_1 - t_0)] = \frac{L_r}{nV_{Cc}T_s} \frac{1}{Z_r} \sqrt{{r_2}^2 - \left(\frac{V_s}{2} - \Delta V_{Cr} - nV_{Cc} \right)^2} = \frac{2}{M_b V_s} \sqrt{-\frac{L_r P_s}{T_s}(1 - M_b)}. \quad (42)$$

Substituting (36), (42), into (41), we are able to obtain ZVS region of the switches in backward direction according to the value of $L_{m1,2}$, P_s, and M_b as in Fig. 13. Larger $L_{m1,2}$ reduces the ZVS region of the proposed converter. However, smaller $L_{m1,2}$ generates high peak in $i_{Lm1,2}$ and disturbs ZCS. In

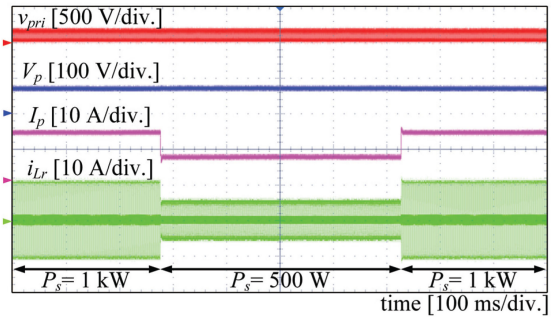

(a)

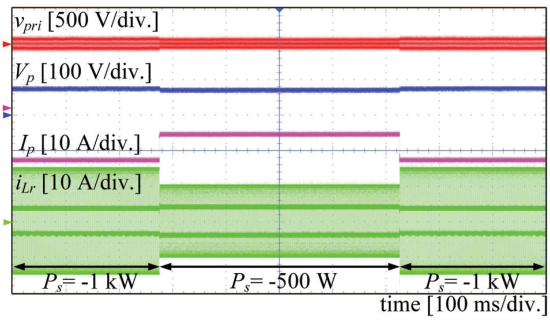

(b)

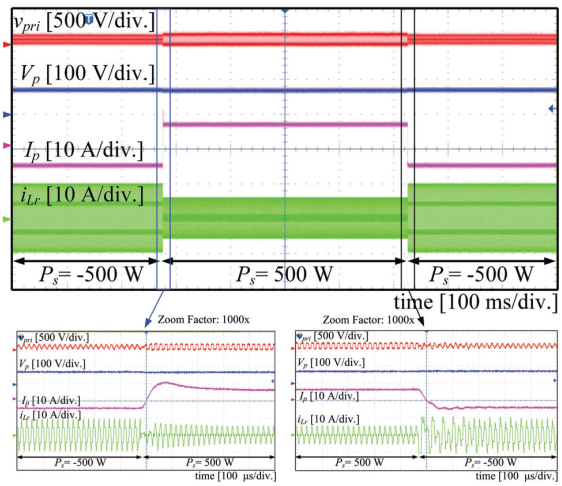

(c)

Fig. 23. Experimental waveforms of v_{pri}, V_p, I_p, and i_{Lr} when the step change in output power occurs at $V_p = 72$ V and $V_s = 380$ V. (a) Load transient in forward mode. (b) Load transient in backward mode. (c) Load transient from backward mode to forward mode and vice versa.

backward direction, we selected the value of $L_{m1,2}$, which has acceptable ZVS region and generates low peak in $i_{Lm1,2}$.

C. Resonant Inductance and Resonant Capacitance

To ensure the proper resonant power transfer, the voltage across the resonant capacitor must be lower than half of the secondary source voltage for all operating conditions, i.e.,

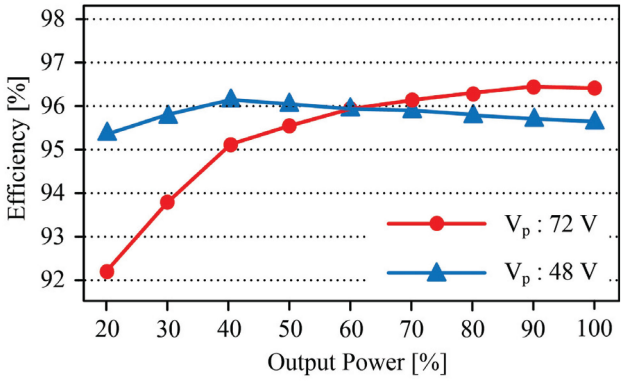

(a)

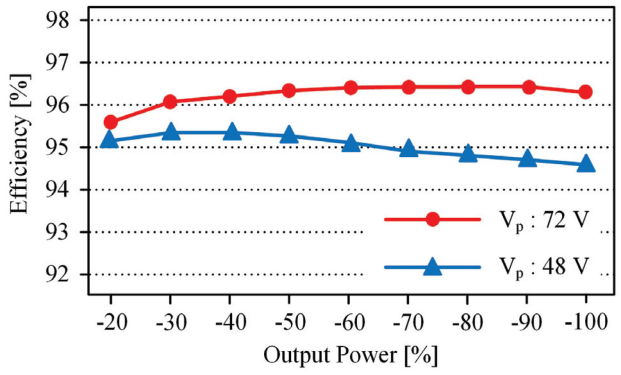

(b)

Fig. 24. Measured efficiency curves of the proposed converter for various ranges of battery voltages according to the output power. (a) Forward mode. (b) Backward mode.

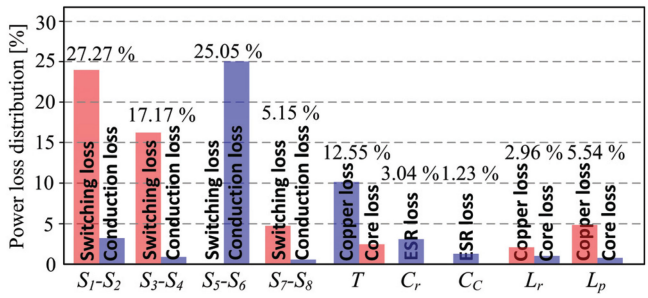

(a)

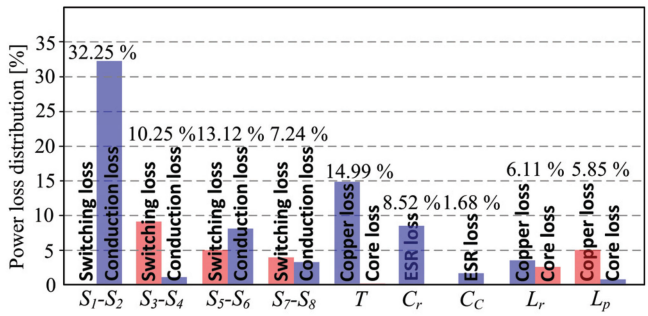

(b)

Fig. 25. Power loss breakdown of the proposed converter at $V_p = 72$ V and full load. (a) Forward mode. (b) Backward mode.

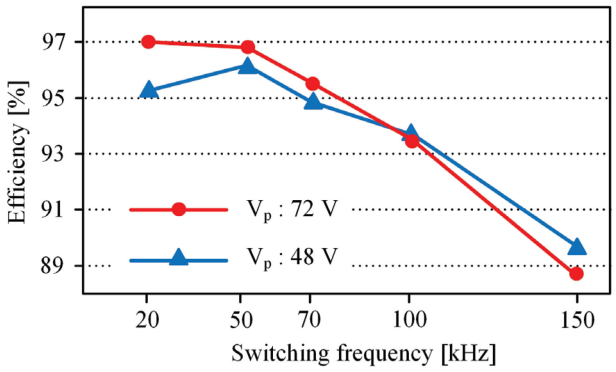

(a)

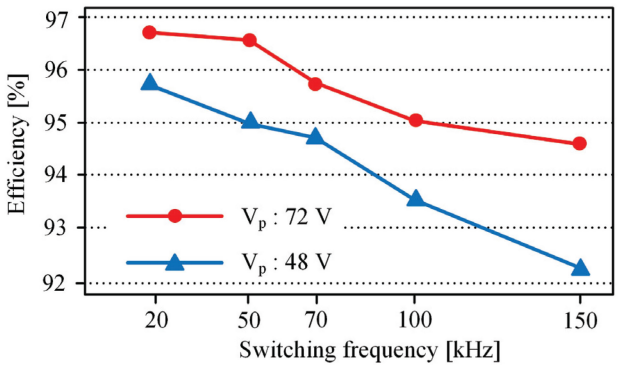

(b)

Fig. 26. Calculated efficiency curves of the proposed converter at full-load across a range of switching frequencies. (a) Forward mode. (b) Backward mode.

$\Delta V_{Cr} \leq V_s/2$, from which we can drive

$$C_r \geq \frac{|P_s|T_s}{V_s^2}. \tag{43}$$

Since large P_s increases the capacitor voltage fluctuation, the capacitor value must be large enough to satisfy (43). Using (8) and (43) yields

$$L_r \leq \frac{V_s^2}{\omega_r^2 |P_s| T_s}. \tag{44}$$

At higher rated power P_s, L_r needs to be lower. But considering the peak current stress, L_r value should be as large as possible.

D. Ripple of Primary Inductor

Let us define $V_{Lm'i'}$ as the voltage across the magnetizing inductor $L_{m'i'}$ $(i = 1, 2)$. In forward operation, the duty-cycle of primary-side switches are fixed to be 0.5 and so the values of V_{Cc}= $2V_p$. The voltage applied to the primary inductor L_p at the steady state is $V_p - V_{Lm2}$ during first half switching period and $V_p - V_{Lm1}$ during second half switching period. The proposed current-fed push–pull resonant converter has theoretically the same values of L_{m1} and L_{m2}; V_{Lm2}=$V_{Cc}/2$=V_p during first half switching period and V_{Lm1}=$V_{Cc}/2$=V_p during second half switching period. Thus, the voltage across L_p at the steady state becomes zero. As a result, the ripple of the primary inductor current is theoretically zero in forward operation.

In backward operation, the voltage across L_p at the steady state is $V_{Cc}/2 - V_p$ during $0 < t < (D_b + D_{bz})T_s$ and $V_{Cc} - V_p$ during $(D_b + D_{bz})T_s \leq t < (1/2 - D_b - D_{bz})T_s$. The ripple of the primary inductor current becomes

$$\begin{aligned}\Delta I_p &= \frac{\left(\frac{V_{Cc}}{2} - V_p\right)(D_b + D_{bz})\,T_s}{L_p} \\ &= \frac{\left(\frac{V_{Cc}}{2} - V_p\right)\left(D_b + \frac{2}{M_b V_s}\sqrt{-\frac{L_r P_s}{T_s}(1 - M_b)}\right)T_s}{L_p}.\end{aligned} \tag{45}$$

E. Switch Consideration

The maximum drain-source voltage stress determines the voltage rating of the switch. The maximum current stress also determines the current rating of the switches. Both stresses are listed in Table I.

VII. Experimental Results

To evaluate the efficiency of the proposed converter, we conducted experimental tests using a 1-kW converter prototype (see Fig. 14, Table II). We selected the primary source voltage $48 \leq V_p \leq 72$ V; secondary source voltage V_s=380 V, and output power P_s=1 kW. The PWM duty control functions were implemented on a TMS320F28377D digital signal processor.

In the forward direction, the converter operates as a PWM push–pull resonant-boost converter. As S_8 is turned ON, the resonant inductor current increases linearly. When S_7 is turned OFF, the resonant inductor current decreases following the downhill part of sinusoidal curve (see Fig. 15). When S_7 is turned OFF, v_{ds7} is very small. Thus, the switch S_7 are turned OFF with almost ZVS (see Fig. 16). Before S_2 and S_3 are turned ON, the negative currents flow through S_2 and S_3, which fully discharge the parasitic capacitances of S_2 and S_3. Then, S_2 and S_3 are turned ON with ZVS (see Figs. 17 and 18). The waveforms of the circuit in the first half period are symmetric and essentially the same as those in the next half switching period. So, S_8 also is turned OFF with almost ZVS and S_1 and S_4 are turned ON with ZVS in the second half of the switching period.

In the backward direction, the converter operates as a half-bridge resonant-buck converter. As S_6 is turned ON, the current begins to flow through L_r and follows a sinusoidal curve. When S_6 is turned OFF and S_8 is turned ON, i_{Lr} goes to zero linearly (see Fig. 19). The switch S_5 is turned OFF with almost ZVS (see Fig. 20). S_3 and S_7 are turned ON with ZVS (see Figs. 21 and 22). Due to the symmetric operation, the switch S_6 also is turned OFF with almost ZVS and the switches S_4 and S_8 also are turned ON with ZVS in the next half switching period.

To show the dynamic performance of the proposed converter, we varied the reference output power from 1 kW to 500 W and vice versa in both power flow directions (see Fig. 23). The primary-side current occasionally experienced an overshoot at

TABLE I
MAXIMUM CURRENT STRESS AND VOLTAGE STRESS ON THE SWITCHES OF THE PROPOSED CONVERTER

Switch	Mode	Current /Voltage	Values
S_1, S_2	Forward	$I_{S1,2,peak}$	$\frac{V_{Cc}}{2L_{m2}} + \frac{P_s}{2V_p} + \frac{r_1}{Z_r}\sin(\alpha + w_r(t-t_1))$
		$V_{S1,2,peak}$	V_{Cc}
	Backward	$I_{S1,2,peak}$	$\frac{nr_2}{Z_r}\sin(w_r(t-t_0)) - \frac{V_{Cc}}{2L_{m1}} - \frac{P_s}{2V_p}$
		$V_{S1,2,peak}$	V_{Cc}
S_3, S_4	Forward	$I_{S3,4,peak}$	$\frac{V_{Cc}}{2L_{m1}} + \frac{P_s}{2V_p}$
		$V_{S3,4,peak}$	V_{Cc}
	Backward	$I_{S3,4,peak}$	$\frac{P_s}{V_p} + \frac{V_{Cc}-V_p}{2L_p}(t_3 - t_2)$
		$V_{S3,4,peak}$	V_{Cc}
S_5, S_6	Forward	$I_{S5,6,peak}$	$\frac{r_1}{Z_r}\sin(\alpha + w_r(t-t_1))$
		$V_{S5,6,peak}$	V_s
	Backward	$I_{S5,6,peak}$	$-\frac{r_2}{Z_r}\sin(w_r(t-t_0))$
		$V_{S5,6,peak}$	V_s
S_7, S_8	Forward	$I_{S7,8,peak}$	$\frac{nV_{Cc}D_fT_s}{L_r}$
		$V_{S7,8,peak}$	$\frac{V_s}{2} + \Delta V_{Cr}$
	Backward	$I_{S7,8,peak}$	$-\frac{r_2}{Z_r}\sin(w_r D_b T_s)$
		$V_{S7,8,peak}$	$\frac{V_s}{2} + \Delta V_{Cr}$

$I_{S'i,'peak}$ is maximum current stress applied to the ith switch.
$V_{S'i,'peak}$ is maximum voltage stress applied to the ith switch.

TABLE II
PARAMETERS AND COMPONENTS OF THE PROTOTYPE

Parameters	Symbols	Value
Primary-side voltage source	V_p	48−72 V
Secondary-side voltage source	V_s	380 V
Rated output power	P_s	1 kW
Switching frequency	f_s	50 kHz
Resonant frequency	f_r	62.91 kHz
Primary inductor	L_p	65 μH
Secondary-side capacitor	C_s	20 μF
Active clamp capacitor	C_c	20 μF
Magnetizing inductance	L_{m1}, L_{m2}	10 μH
Resonant inductance	L_r	32 μH
Transformer turns ratio	N_{p1}:N_{p2}:N_s	5:5:12
Resonant capacitance	C_{r1},C_{r2}	100 nF
Components	**Symbol**	**Part number**
Primary-side switch	S_1-S_4	IPP051N15N5
Secondary-side switches	S_5-S_8	UJC06505K
Transformer core	T	PQ5050

the transient, but it was not so large enough to destroy the active power components.

The power conversion efficiency was measured by Yokogawa WT1800 digital power meter. The maximum measured efficiency was 96.85% in the forward direction [see Fig. 24(a)] and 96.44% in the backward direction [see Fig. 24(b)]. Power loss distributions of the proposed converter are obtained in both power flow directions at full load. In Fig. 25(a), each loss occurred at the primary-side switches and the secondary-side switches takes 44.44% and 30.20% of the total loss in forward mode, respectively. In Fig. 25(b), the conduction loss occurred at the primary-side switches S_1 and S_2 occupies 36.97% of the total power loss in backward mode, because the body diodes of S_1 and S_2 conduct during the backward power transfer.

We have calculated the efficiency of the proposed converter at full-load across a range of switching frequencies from 20 to 150 kHz (see Fig. 26). As the switching frequency increases, the calculated efficiency becomes lower because the primary inductor current generates offset current at the switches; this offset current incurs the switching loss at every switching instant. This switching loss is inevitable in the current-fed type converter. However, the proposed converter can achieve almost ZVS turn OFF at S_7 and S_8 in forward direction and S_5 and S_6 in backward direction. This aspect ensures relatively high efficiency upto 100 kHz.

We have compared proposed topology with existing ones in terms of the number of power components, operation modes, power conversion efficiency, input/output voltages, and rated power (see Table III). In bidirectional current-fed push–pull converters, the current mismatch between the primary-side inductor and leakage inductance of the transformer generates a large voltage overshoot at the primary-side switching devices. This problem can be alleviated with the resonant active-clamp circuit [21]. However, two resonant active-clamp circuits are required for bidirectional power transfer. These circuits include many power components and so complicate the overall circuit design. By using secondary-side switches and their modulation [22], [23], the bidirectional current-fed push–pull converters naturally clamp the voltage at the primary-side switches without using additional snubber circuits. Therefore, this aspect reduces the required number of power components. However, the large amount of reverse current flows through the secondary-side switches. This current enables ZVS turn ON of the secondary-side switches, but increases the conduction loss occurred at the secondary-side switches significantly. The current-fed push–pull resonant converter [20] transfers the power in resonant way and so achieve ZCS turn OFF of the secondary-side switches when the voltage gain is unity. This circuit does not experience the reverse current at the secondary-side switches. However, this circuit suffers from hard switching turn OFF at the secondary-side

TABLE III
COMPARISON OF CONVENTIONAL PUSH–PULL CONVERTERS AND PROPOSED CONVERTER

Items		[21]	[22, 23]	[20]	Proposed converter
Topology		Current-fed push-pull + resonant active-clamp	Current-fed push-pull	Current-fed resonant push-pull	Current-fed resonant push-pull + bidirectional switch
Current waveforms		Linear	Linear	Resonant	Resonant
Number of components	Switches	6	4 / 6	6	8
	Inductors	1	1	2	2
	Capacitors	0	2	3	3
	Transformer	1	1	1	1
Auxiliary components		Two resonant active-clamp circuits	-	-	-
Peak efficiency in forward mode		94.5%	94.8% / 96.3%	N/A	96.85%
Peak efficiency in backward mode		94.8%	N/A / 96.3%	95.9%	96.44%
Input voltage		12 V	22–41 V / 20–30 V	50–60 V	48–72 V
Output voltage		400 V	200 V / 400 V	660 V	380 V
Rated power		1.5 kW	250 W / 300 W	5 kW	1 kW
Switching frequency		70 kHz	100 kHz	50 kHz	50 kHz
Turn-off voltage on secondary-side switches		V_s	V_s	V_s	$V_s/2 - \Delta V_{Cr}$

Note: N/A stands for not available,

switches when the voltage gain is far away from unity. By using the bidirectional switch at the secondary side, the proposed converter can achieve almost ZVS turn OFF at the secondary side of the switches irrespective of the voltage gain. This aspect reduces the switching loss significantly and increases the power conversion efficiency of the converter.

VIII. CONCLUSION

This article has presented bidirectional push–pull resonant converter that has minimized switching loss over wide range of input voltages. The converter is applicable to the energy storage systems. The proposed converter consists of a current-fed push–pull circuit on the primary side and an active voltage doubler circuit with a bidirectional switch on the secondary side. The converter operates as a PWM push–pull resonant-boost converter during a forward mode operation, and as a PWM half-bridge resonant-buck converter during backward-mode operation. This topology and corresponding switching modulation naturally yield almost ZVS turn OFF of switches, and thereby ensures high-power conversion efficiency even under high-frequency operation; these traits reduce the size and cost of the fabricated converter. The proposed converter does not suffer from instantaneous reactive current under the wide voltage variations, so the power conversion efficiency is very high. Moreover, the converter accomplishes a high conversion ratio in both power flow directions without using a transformer that has high turns-ratio. A 1-kW prototype converter is build and used to confirm the superior performance of the proposed converter. Given the designated power and input voltage ranges, the peak efficiency reaches 96.85% in forward direction and 96.44% in the backward direction.

REFERENCES

[1] "Storage and renewables: Costs and markets to 2030," Abu Dhabi, UAE: IRENA, 2017.
[2] D. Proctor, "Research group: Energy storage market will hit $546 billion by 2035," Lux Research, 2020. [Online]. Available: https://www.powermag.com/research-group-energy-storage-market-will-hit-546-billion-by-2035/
[3] N. M. Mukhtar and D. D. C. Lu, "A bidirectional two-switch flyback converter with cross-coupled LCD snubbers for minimizing circulating current," *IEEE Trans. Ind. Electron.*, vol. 66, no. 8, pp. 5948–5957, Aug. 2019.
[4] K. S. Kim, S. H. Lee, W. J. Cha, J. M. Kwon, and B. H. Kwon, "Bidirectional single power-conversion DC-AC converter with noncomplementary active-clamp circuits," *IEEE Trans. Ind. Electron.*, vol. 63, no. 8, pp. 4860–4867, Aug. 2016.
[5] H. H. Chung, W. L. Cheung, and K. S. Tang, "A ZCS bidirectional flyback DC/DC converter," *IEEE Trans. Ind. Electron.*, vol. 19, no. 6, pp. 1426–1434, Nov. 2004.
[6] C. L. Shen, H. Liou, T. C. Liang, and H. Z. Gong, "An isolated bidirectional interleaved converter with minimum active switches and high conversion ratio," *IEEE Trans. Ind. Electron.*, vol. 65, no. 3, pp. 2313–2321, Mar. 2018.
[7] N. M. Mukhtar and D. D. C. Lu, "An isolated bidirectional forward converter with integrated output inductor-transformer structure," in *Proc. IEEE 4th Southern Power Electron. Conf.*, 2018 pp. 1–7.
[8] M. Khodabakhshian, E. Adib, and H. Farzanehfard. "Forward-type resonant bidirectional DC-DC converter," *IET Power Electron.*, vol. 9, no. 8, pp. 1753–1760, Jun. 2016.
[9] L. Huang, Z. Zhang, and M. A. Andersen, "Analytical switching cycle modeling of bidirectional high-voltage flyback converter for capacitive load considering core loss effect," *IEEE Trans. Power Electron.*, vol. 31, no. 1, pp. 470–487, Jan. 2016.

[10] P. Thummala, D. Maksimovic, Z. Zhang, and M. A. Andersen, "Digital control of a high-voltage (2.5 kV) bidirectional DC–DC flyback converter for driving a capacitive incremental actuator," *IEEE Trans. Power Electron.*, vol. 31, no. 12, pp. 8500–8516, Dec. 2016.
[11] D. R. Nayanasiri, D. M. Vilathgamuwa, D. L. Maskell, and G. F. H. Beng, "Soft-switching single inductor current-fed push-pull converter for PV applications," in *Proc. IECON 40th Annu. Conf. IEEE Ind. Electron. Soc.*, Oct./Nov. 2014, pp. 5589–5594.
[12] S. Li, K. Xiangli, and K. M. Smedley, "A control map for a bidirectional PWM plus phase-shift-modulated push-pull DC-DC converter," *IEEE Trans. Ind. Electron.*, vol. 64, no. 11, pp. 8514–8524, Nov. 2017.
[13] K. R. Sree and A. K. Rathore, "Impulse commutated zero-current switching current-fed push-pull converter: Analysis, design, and experimental results," *IEEE Trans. Ind. Electron.*, vol. 62, no. 1, pp. 363–370, Jan. 2015.
[14] S. Lee, J. Park, and S. Choi, "A three-phase current-fed push-pull DC-DC converter with active clamp for fuel cell applications," *IEEE Trans. Power Electron.*, vol. 26, no. 8, pp. 2266–2277, Aug. 2011.
[15] R. L. Andersen and I. Barbi, "A ZVS-PWM three-phase current-fed push-pull DC-DC converter," *IEEE Trans. Ind. Electron.*, vol. 60, no. 3, pp. 838–847, Mar. 2013.
[16] M. Kwon, J. Park, and S. Choi, "A bidirectional three-phase push-pull converter with dual asymmetrical PWM method," *IEEE Trans. Power Electron.*, vol. 31, no. 3, pp. 1887–1895, Mar. 2016.
[17] T. T. Le, H. Jeong, and S. Choi, "A bidirectional three-phase push-pull converter with hybrid PPS-DAPWM switching method for high power and wide voltage range applications," *IEEE Trans. Ind. Electron.*, vol. 68, no. 2, pp. 1322–1331, Feb. 2021.
[18] S. Bal, A. K. Rathore, and D. Srinivasan, "Naturally clamped snubberless soft-switching bidirectional current-fed three-phase push-pull DC-DC converter for DC microgrid application," *IEEE Trans. Ind. Appl.*, vol. 52, no. 2, pp. 1577–1587, Mar./Apr. 2016.
[19] E. H. Kim and B. H. Kwon, "High step-up resonant push-pull converter with high efficiency," *IET Power Electron.*, vol. 2, no. 1, pp. 79–89, Jan. 2009.
[20] J. Hiltunen, V. Väisänen, and P. Silventoinen, "A bidirectional current-fed resonant push-pull converter for low voltage, high current applications," in *Proc. IEEE Energy Convers. Congr. Expo.*, 2013, pp. 4770–4774.
[21] M. Cacciato, A. Consoli, V. Crisafulli, G. Vitale, and N. Abbate, "A new resonant active clamping technique for bi-directional converters in HEVs," in *Proc. IEEE Energy Convers. Congr. Expo.*, 2010, pp. 1436–1441.
[22] P. Xuewei and A. K. Rathore, "Current-fed soft-switching push-pull front-end converter-based bidirectional inverter for residential photovoltaic power system," *IEEE Trans. Power Electron.*, vol. 29, no. 11, pp. 6041–6051, Nov. 2014.
[23] R. Kosenko, A. Chub, and A. Blinov, "Full-soft-switching high step-up bidirectional isolated current-fed push-pull DC-DC converter for battery energy storage applications," in *Proc. IECON 42nd Annu. Conf. IEEE Ind. Electron. Soc.*, 2016, pp. 6548–6553.

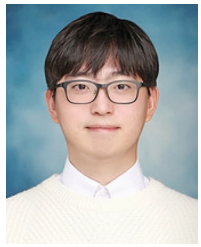

Jong-Won Lim (Student Member, IEEE) was born in Busan, South Korea, in 1994. He received the B.S. degree in electronic and electrical engineering in 2020 from Dongguk University, Seoul, South Korea, where he is currently working toward the M.S. degree in electronics and electrical engineering.

His research interests include power conversion systems, high-efficient power circuit design, and bidirectional converter.

Jamil Hassan (Student Member, IEEE) was born in Skardu Gilgit, Baltistan, Pakistan, in 1998. He received the B.S. degree in electrical in power engineering from COMSATS University Islamabad, Islamabad, Pakistan, in 2019. He is currently working toward the M.S. degree in electronics and electrical engineering with Dongguk University, Seoul, South Korea.

His research interests include power conversion systems, high-efficient power circuit design, and bidirectional converter.

Minsung Kim (Senior Member, IEEE) was born in Ulsan, Korea, in 1986. He received the B.S. and Ph.D. degrees in electrical engineering from Pohang University of Science and Technology (POSTECH), Pohang, South Korea, in 2008 and 2013, respectively.

Since 2013, he has been with the Department of Creative IT Engineering and Future IT Research Laboratory, POSTECH, where he is currently a Research Assistant Professor. In 2016, he was also a Research Scholar with Future Energy Electronics Center, Virginia Tech, Blacksburg, VA, USA. In 2017, he was also an Academic Visitor with Control and Power System Group, Imperial College London, London, U.K. Since 2018, he has been with the Division of Electronics and Electrical Engineering, Dongguk University, Seoul, South Korea, where he is currently an Assistant Professor. His research interests include highly efficient power conversion circuit design, and intelligent controller design for industrial electronics, and renewable energy and energy storage systems.